BMC Biology

RESEARCH ARTICLE Open Access

SUGAR-seq reveals the transcriptome and N-linked glycosylation landscape of mononuclear phagocytes at single-cell resolution in a mouse model of autosomal dominant osteopetrosis type 2

Yu Sha[1†], Lingyu Huang[1†], Lei Zhang[3†], Xianliang Hou[1], Chune Mo[1], Cuiping Pan[1], Gengshuo Chen[1], Sha Luo[1] and Minglin Ou[1,2*]

Abstract

Background Heterozygous mutation of CLCN7 (R286W) is commonly found in patients with benign autosomal dominant osteopetrosis. However, there is no evidence from animal models to confirm that it is a disease mutation. And the characteristics of the bone marrow cell (BMC) landscape in osteopetrosis at the single-cell level are completely unknown till now.

Results In this study, we generated the first autosomal dominant osteopetrosis type 2 (ADO2) mouse model with typical phenotypes carried a mutation Clcn7 (r284w) corresponding to CLCN7 (R286W) observed in human patients using gene editing technology. And then, we conducted the first-ever single-cell analysis of the RNA expression and N-linked glycosylation profiles for the mouse BMCs by SUrface-protein Glycan And RNA-sequencing (SUGAR-seq). We identified 14 distinct cell types and similar proportion of neutrophils in both ADO2 and wild type mice, confirmed by flow cytometry analysis. The N-linked glycosylation modifications of BMCs were significantly downregulated detecting by SUGAR-seq, which was similar to the situation of N-Glycan profiling by the 4D Label-Free N-Glycosylation Proteomics Analysis. Particularly noteworthy is the heterogeneity of classic monocytes. We identified six cell subtypes, but only two cell subtypes were found with different proportion of cell, whose different expressed genes were associated with NF-κB-inducing kinase / Nuclear Factor-kappa B (NIK/NF-κB) signaling and other pathway associated with osteoclast differentiation.

Conclusions Our murine model confirms that the human CLCN7 (R286W) is a pathogenic mutation for ADO2. Additionally, our single-cell analyses reveal the heterogeneity of monocytes in ADO2, and the abnormal glycosylation modifications across various subtypes may represent important events in the pathogenesis of osteopetrosis.

Keywords Osteopetrosis, Single-cell resolution, Mononuclear phagocytes, Glycoproteome

†Yu Sha, Lingyu Huang and Lei Zhang contributed equally to this work.

*Correspondence:
Minglin Ou
minglinou@glmc.edu.cn; minglinou@163.com
Full list of author information is available at the end of the article

Background

Osteopetrosis is a rare genetic bone disorder characterized by diffuse skeletal sclerosis caused by abnormal bone metabolism [1–3]. The incidence of this disorder is approximately 1:100,000–1:50,000 [4, 5]. There are three clinically and genetically distinct forms of osteopetrosis, namely, adult benign autosomal dominant osteopetrosis, intermediate autosomal recessive osteopetrosis, and infantile malignant autosomal recessive osteopetrosis [1]. The most common type is autosomal dominant osteopetrosis type 2 (ADO2), associated with CLCN7 mutations [3]. At present, there are no definitive cures for osteopetrosis and only symptomatic treatment can be used to delay disease progression, such as preventing fractures, blood transfusions, controlling infections, alleviating nerve compression, and so on [6].

Previous work has shown that rs1291061962 CLCN7 (R286W) may be one of the most common mutations in ADO2, and our previous studies also confirmed that this mutation could be found in Chinese familial ADO2 patients who exhibited typical abnormal bone metabolism symptoms, such as increased whole-body bone density, multiple fractures, and narrowing of the bone marrow cavity [3, 6–11]. The heterozygous mutation of CLCN7 (R286W) may damage the structure of ClC-7 predicted by bioinformatics and it supposed to be the main causes of abnormal bone metabolism in ADO2 [3, 6, 10, 12]. However, there is no evidence of animal model study till now.

Some studies have indicated that the bone-resorbing cells, such as osteoclasts, play key roles in ADO2 [13–15]. It is originated from the mononuclear phagocyte lineage of cells in the bone marrow cavity. As we known, the types, relative numbers, and surface modifications of the cells in the bone cavity are important factors to maintain the bone marrow microenvironment. Recently, papers documents that glycosylation, especially N-linked glycosylation, is one of the most common posttranslational protein modifications in eukaryotic cells, and it plays multiple biological functions and cell–cell communication and cellular signaling [16–20]. Interesting, evidences have also confirmed that protein glycosylation participates in the regulation of osteoclast and osteoblast activities, which is very important in bone resorption and bone formation [21–24]. Therefore, the landscaping the microenvironment in the bone marrow cavity at the single-cell level is necessary for understanding the pathological mechanism of osteopetrosis.

Recently, SUrface-protein Glycan And RNA-sequencing (SUGAR-seq) has emerged as a powerful approach for accurate quantification of cell glycosylation level together with gene expression profiles on the single-cell level by chemoenzymatic method where ProMoSCOPE tag covalently binds to N-Acetyllactosamine (LacNAc) at cell surface [25–29].

Therefore, this study aims to use Clustered Regularly Interspaced Short Palindromic Repeats / CRISPR-associated protein 9 (CRISPR/Cas9) technology to develop a mouse model harboring the Clcn7(r284w) corresponding to CLCN7 (R286W) mutation observed in human and analyze its phenotypes to confirm if it is a disease mutation for osteopetrosis for ADO2. And then we try to landscape the microenvironment of bone marrow cavity, including the consist of cell types, relative numbers, modifications of N-linked glycosylation and gene expression at the single-cell level by SUGAR-seq, which may be valuable for further investigation of the pathogenesis of osteopetrosis pathogenesis, development of therapeutic strategies, and related drug discovery.

Results

Generation and characteristic analysis of the ADO2 mouse model

To generate the ADO2 mouse model, we amplified the target region of the CLCN7 locus in mice using specific primers and confirmed successful targeting by sequencing PCR product. Subsequently, the 632-bp PCR product obtained from agarose gel electrophoresis was collected for verification by Sanger sequencing, which confirmed the presence of a mutation of CGG to TGG to generate Clcn7 (R284W) (Fig. 1a).

Using the IVIS Lumin XRMS Series III In Vivo Imaging Device with the "X-ray" module (parameters: V220-240, Hz50-60), we compared ADO2 mice with age-matched WT mice (7 weeks old). The ADO2 mice exhibited a reduction in the medullary cavity volume and a significant increase in X-ray grayscale, indicating higher bone density (Fig. 1b).

We performed HE staining on bone marrow sections of 7-week-old ADO2 and wild-type (WT) mice. The ADO2 mice exhibited generally normal bone marrow hematopoietic tissue, slightly thickened cortical bone, thicker trabeculae, and essentially normal bone marrow hematopoietic tissue (Fig. 1c). Additionally, scattered incompletely ossified cartilage matrices were observed in the trabeculae and cortical bone near the epiphyseal end of the femur. Then, multiple measurements were taken at different locations along the femoral diaphysis, including both the thickest and thinnest regions, and we calculated the mean and standard deviation for each group. The results showed that the thickest point in ADO2 mice was 193.08 ± 11.99 μm, and the thinnest point was 131.10 ± 14.31 μm. In contrast, WT mice had a maximum thickness of 162.08 ± 7.78 μm and a minimum thickness of 83.43 ± 21.14 μm, indicating that the cortical bone in ADO2 is thicker compared to WT. Notably, these

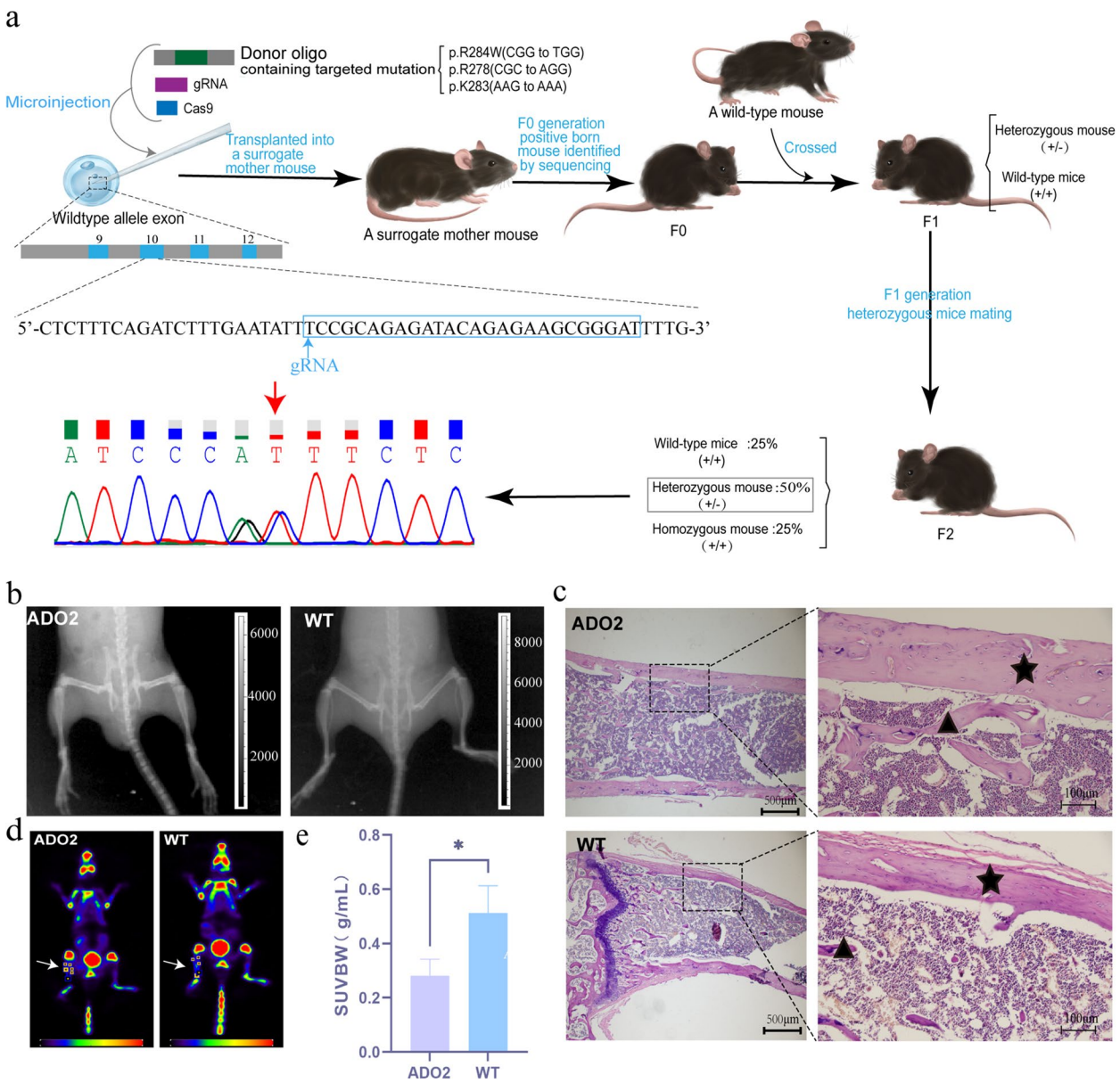

Fig. 1 Generation of the ADO2 mouse model and characterization of disease features. **a** Process of the ADO2 mouse model construction and Sanger sequencing chromatogram confirming the p.R284W (CGG to TGG) mutation. **b** X-ray examination of ADO2 heterozygous mice and WT mice revealing increased cortical bone thickness and narrowed bone marrow space in ADO2 heterozygous mice. **c** Histological examination of femur bone sections stained with hematoxylin and eosin (HE) showing increased cortical bone thickness (indicated by asterisks) and thicker trabeculae (indicated by triangles) in ADO2 heterozygous mice compared to WT mice. **d** Region of interest (ROI) outlined on the maximum intensity projection (MIP) image from PET imaging, depicting the left tibia in ADO2 and WT mice for sodium fluoride metabolism imaging with PET/CT. **e** In ADO2 mice ($N=3$), the maximum standardized uptake value (SUVmax) was significantly lower than that in WT mice ($N=3$), with statistical significance determined using a *t* test (* $P<0.05$)

findings align with our X-ray observations, confirming the thickened bone cortex in ADO2 mice.

To investigate differences in bone metabolism between ADO2 and wild-type mice, we used positron emission tomography/computed tomography (PET/CT) imaging to assess the metabolism of ^{18}F-NaF in both groups. The PET/CT fusion images were processed using PMOD 4.3 software. Subsequently, we identified the region of interest in the left tibias of the mice (Fig. 1d) and calculated the maximum standardized uptake value (SUVmax) as an indicator of bone metabolism. After excluding the maximum and minimum values from both the ADO2 and

WT groups, we performed *t* tests on the remaining three datasets from each group (Additional File 2: Table S1). The results revealed a significant difference ($P<0.05$) in SUVmax between the two groups (Fig. 1e), with the SUVmax of ADO2 mice (0.282 ± 0.061) significantly lower than that of WT mice (0.512 ± 0.101). Therefore, we concluded that the bone metabolism of ADO2 mice is significantly slower than that of WT mice.

The above results indicate that the gene-edited mice exhibited typical symptoms of osteopetrosis, such as bone marrow cavity narrowing, increased cortical thickness, and abnormal bone metabolism, which confirms the successful establishment of the ADO2 mouse model [3, 12].

Heterogeneity analysis of BMCs in ADO2 mice using SUGAR-seq

We employed a combined the RNA expression profiles and the cell surface features of N-linked glycosylation approach using SUGAR-seq to analyze the transcriptional profiles and cell surface glycan abundance in ADO2 mouse bone marrow cells (Workflow of the SUGAR-seq procedure is shown in Fig. 2).

Based on bone marrow cell marker gene expression, we successfully identified and characterized 14 distinct cellular subpopulations, namely, granulocyte-monocyte progenitor cells (GMP), precursor B cells (Pre_B), erythroid progenitor cells (ProEryth), hematopoietic stem cells (HSCs), mature B cells (MatureB), plasma cells (PlasmaCells), T and NK cells (TandNK), neutrophils, basophils, eosinophils, macrophages, monocytes, conventional dendritic cells (cDCs), and plasmacytoid dendritic cells (pDCs) (Fig. 3a). By utilizing uniform manifold approximation and projection (UMAP) dimensionality reduction analysis, we obtained high-resolution UMAP clustering maps of bone marrow cells taken from ADO2 and WT mice (Fig. 3b). Subsequently, we overlaid these 14 cell clusters onto the UMAP clustering maps to gain comprehensive insights into their distribution patterns in ADO2 mice (Fig. 3c).

After annotating the major cell populations, we obtained the cell counts for each cell cluster, as shown in Table 1 and Fig. 3d. We compared the proportions of each cell type within the total bone marrow cell population between the ADO2 and WT mice with Pearson's chi-square test and found significant differences in the proportions of GMPs, neutrophils, monocytes, TandNK cells, MatureB cells, ProEryth cells, cDCs, and pDCs ($P<0.05$). Specifically, the proportions of neutrophils, GMPs, and ProEryth cells were significantly lower, while the proportions of plasma cells, monocytes, TandNKs, MatureB cells, cDCs, and pDCs were significantly higher in the ADO2 mice than in the WT mice (Table 1). These changes may be attributed to alterations in the bone marrow microenvironment caused by the Clcn7 (r284w) mutation. Additionally, we employed flow cytometry to validate the predominant cell type (neutrophils) in the bone marrow of ADO2 ($N=3$) and WT ($N=3$) mice. The proportion of neutrophils in the ADO2 group was significantly lower than that in the WT group ($P<0.05$) (Fig. 3e, Additional File 2: Table S2). This finding was consistent with the results obtained from SUGAR-seq, providing further confirmation of the reliability of our SUGAR-seq results. Furthermore, we performed scMetabolism analysis on cell clusters, such as GMP and GMP-derived cells (neutrophils and monocytes), which were closely associated with the spectrum of osteoclast differentiation. We found significant alterations in the metabolism of glucose, lipid, energy, glycogen, and vitamin in bone marrow cells of ADO2 mice (Additional file 1: Fig. S1a-c).

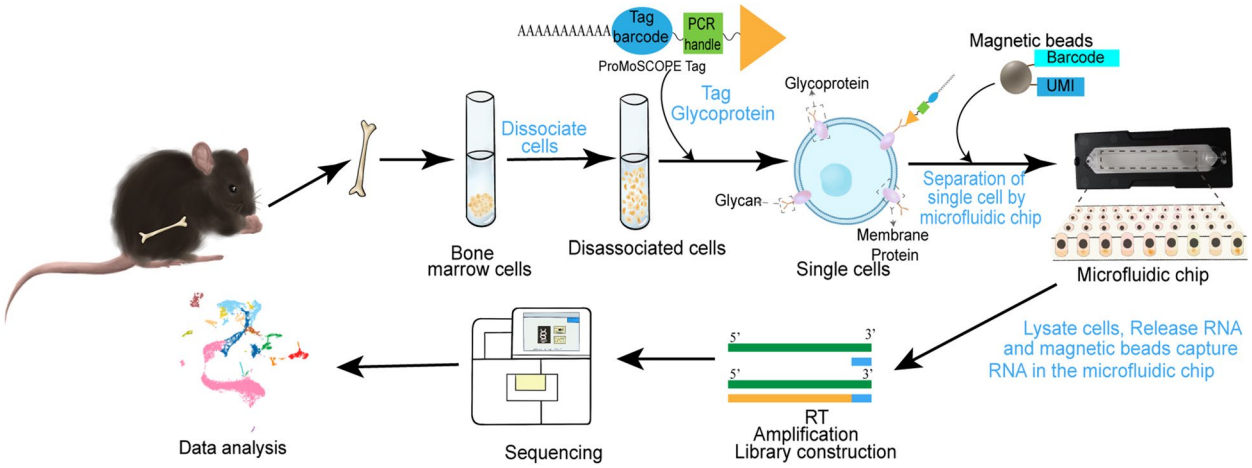

Fig. 2 Workflow of SUGAR-seq procedure for single bone marrow cell analysis in a mouse model

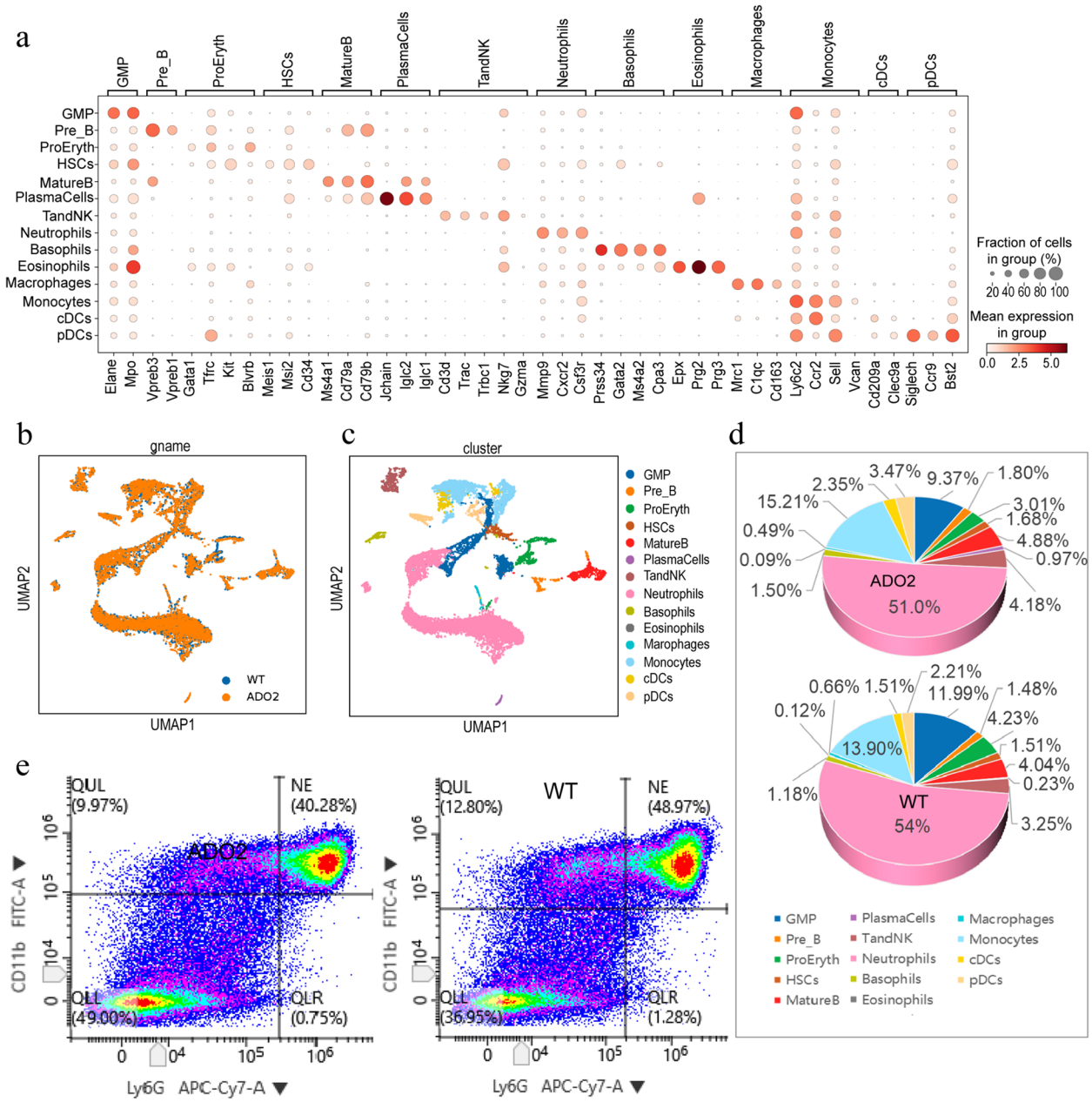

Fig. 3 Overview of cell cluster analysis and distribution across ADO2 and WT groups. **a** Dot plot graph showing the normalized expression levels of marker genes in each of the 14 identified cell clusters. **b** UMAP clustering plots of 13,031 cells from the two groups, which provides an overview of the sample distribution between the ADO2 and WT groups. **c** UMAP plot visualizing the 14 distinct cell types across ADO2 and WT groups, uniquely colored and labeled. **d** Pie charts representing the frequency of cell clusters in the ADO2 and WT groups. Each cluster is colored and labeled, with the area of each sector reflecting its frequency in the respective groups. **e** Pseudocolor plot showing the proportion of neutrophils in bone marrow cells in the ADO2 and WT groups

In addition to transcriptional profiling, we employed SUGAR-seq, a technique based on lectin-mediated N-glycans profiling, to characterize the cell surface N-linked glycosylation at the single-cell level (Fig. 4a). We observed that the total levels of N-linked glycosylation on the surface of all bone marrow cells were significantly lower in ADO2 mouse compared to WT mouse (Fig. 4b). Furthermore, we compared the N-linked glycosylation levels of the cell clusters between the two groups of mice. Interestingly, the total levels of N-glycans on the surface of all bone marrow cells were higher on GMP and ProEryth cells, while that on Pre_B cells, HSCs,

Table 1 Comparison of bone marrow cell proportions between WT and ADO2 groups using the chi-square test

Cluster	WT count	ADO2 count	Chi-square	*P*-value
GMP	722	657	23.420	< 0.001*
Pre_B	89	126	2.401	0.153
ProEryth	255	211	16.260	< 0.001*
HSCs	91	118	0.610	0.435
MatureB	243	342	5.384	0.020*
PlasmaCells	14	68	28.799	< 0.001*
TandNK	196	293	7.683	0.006*
Neutrophils	3233	3575	9.329	0.002*
Basophils	71	105	2.475	0.116
Eosinophils	7	6	0.305	0.581
Macrophages	40	34	1.841	0.175
Monocytes	837	1066	4.457	0.035*
cDCs	91	165	11.928	0.001*
pDCs	133	243	18.305	< 0.001*
SUM	6022	7009		

The chi-square test of fourfold contingency tables was used to compare the cell proportions between the WT and ADO2 groups. SUM represents the total number of cells annotated in the bone marrow. The *p*-value represents the statistical significance of the differences observed (* $P < 0.05$)

MatureB cells, plasma cells, TandNK cells, neutrophils, eosinophils, basophils, macrophages, monocytes, cDCs, and pDCs were lower in ADO2 mice than in WT mice (Fig. 4c).

Our SUGAR-seq data revealed the transcriptional profiles, heterogeneity in surface N-glycosylation levels across cells, and metabolic abnormalities in ADO2 mouse bone marrow cells. These findings revealed that bone marrow cells in ADO2 mice did not exhibit substantial changes in the cell types present, but there were notable variations in the proportions of different cell types and in their metabolism. Furthermore, the observed significant reduction in the level of N-linked glycosylation on the surface of bone marrow cells in ADO2 mice implies that changes in surface N-linked glycosylation levels serve as a crucial pathological feature of osteopetrosis.

Heterogeneity analysis of mononuclear phagocytes in ADO2

The mononuclear phagocyte system (MPS) in the bone marrow plays a critical role in various physiological processes. Composed of immune cells, the MPS is involved in immune responses and inflammation regulation, thus impacting skeletal health. Additionally, MPS cells serve as osteoclast precursor cells, playing a crucial role in osteoclast formation and activation [30–32]. MPS-derived cytokines and signaling molecules, including macrophage-colony stimulating factor (M-CSF) and receptor activator of nuclear factor kappa B ligand (RANKL), play a crucial role in stimulating the proliferation and differentiation of osteoclast precursors, leading to the formation of fully functional mature osteoclasts [33–37]. In our transcriptome profiling data, we identified 251 upregulated and 44 downregulated genes in the macrophages of ADO2 mice (Additional file 1: Fig. S2a). Functional enrichment analysis revealed that the genes downregulated in macrophages were significantly associated with in molecular functions about osteoclast functionality, such as "GDP-dissociation inhibitor activity" and "fatty acid binding" (Additional file 1: Fig. S2b) [38–41].

Given the limited population of macrophages within the bone marrow, our research aimed to investigate the interplay between monocytes and osteoclasts to elucidate their pivotal contributions to the aberrant bone metabolism observed in ADO2 (Fig. 5a). Based on cell surface markers including Ly6c2, Ccr2, Chil3, Ace, Ear2, Eno3, and others, we successfully classified mononuclear cells within the bone marrow of ADO2 and WT mice into distinct subpopulations, referred to as classical monocytes (ClassicalMono) and nonclassical monocytes (NonClassicalMono) (Additional file 1: Fig. S2c). Notably, there was a significantly lower abundance of nonclassical monocytes than of classical monocytes in both the WT and ADO2 mice in our annotated monocyte populations (Fig. 5b). Consequently, our analysis was primarily centered on the classical monocyte subset. Single-cell sequencing results indicated that there was no significant difference in the proportion of classical monocytes within the monocyte population in the bone marrow between the ADO2 and WT groups (Additional File 2: Table S3). This observation was further supported by our flow cytometry analysis (Fig. 5d–g, Additional File 2: Table S4-5). Classic monocytes were further grouped into different subtypes by unsupervised clustering, including ClassicaMo_1 (CM1), ClassicaMo_2 (CM2), ClassicaMo_3 (CM3), ClassicaMo_4 (CM4), ClassicaMo_5 (CM5), and ClassicaMo_6 (CM6) (Fig. 5h). Interestingly, we found a lower proportion of CM2 (20.95% vs. 26.39%) and a higher proportion of CM4 (18.17% vs. 14.08%) in ADO2 mice than in WT mice ($P < 0.05$) (Additional File 2: Table S6). Furthermore, all six classical monocyte subtypes exhibited abnormal expression of integrin-related genes (Table 2). This finding indicates that disease-induced changes in cell type abundance may not be apparent when cells are classified at a high level, but changes in the abundance of specific subgroups can be detected through single-cell analyses, which offer inherent advantages for sensitively detecting such changes and gaining a comprehensive understanding of how osteopetrosis affects cell composition and functionality.

To gain a deeper understanding of the cell subpopulations exhibiting quantitative differences in the

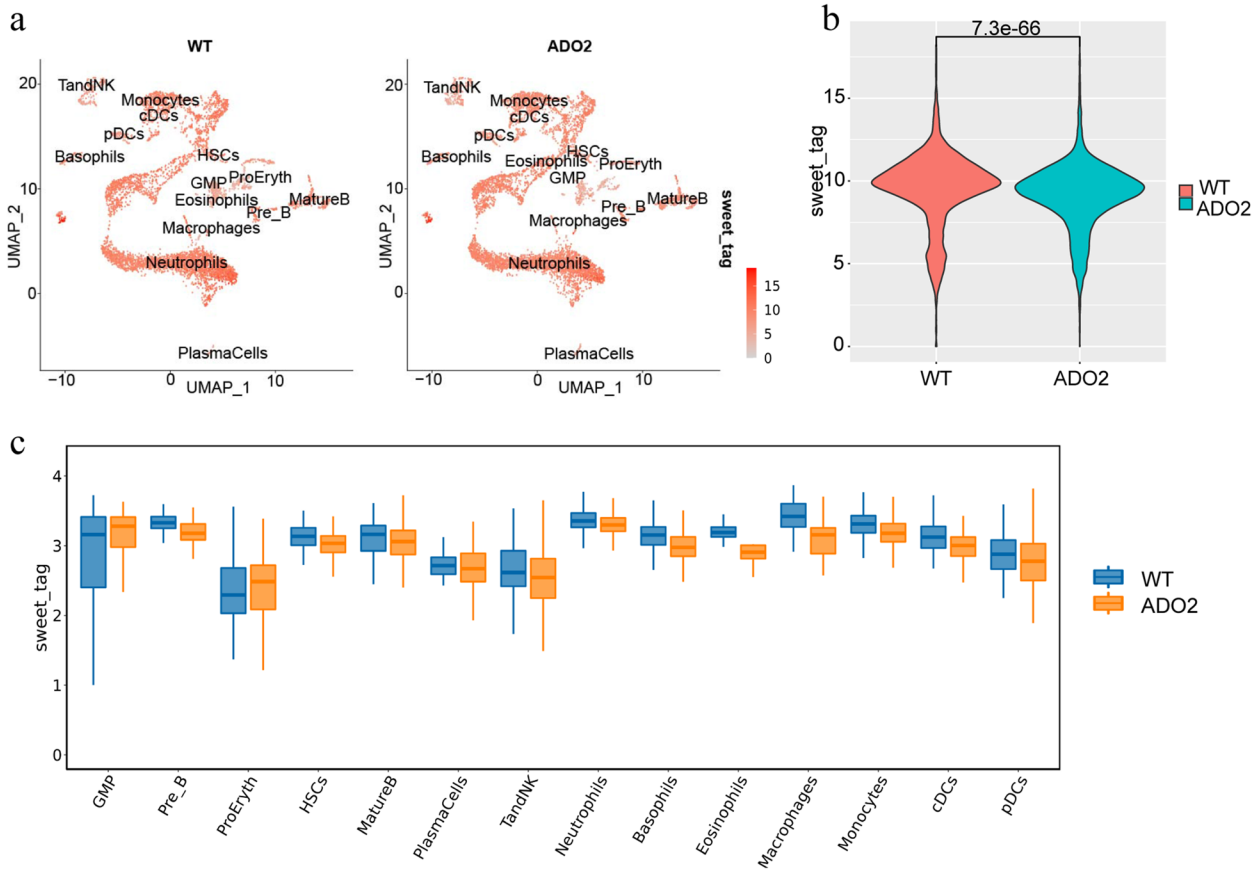

Fig. 4 Visualization analysis of surface N-glycosylation levels comparing ADO2 and WT cell groups. **a** Featureplot UMAP visualization comparing the surface N-glycan abundance between the ADO2 and WT cell groups. Each data point represents a cell, with the color shade indicating the level of cell surface N-glycans. **b** Violin plot showing the significantly lower overall cell surface N-linked glycosylation level in the ADO2 group than in the WT group ($P < 0.05$). **c** Boxplot illustrating variations in overall cell surface N-linked glycosylation level across the 14 cell clusters between the ADO2 and WT groups

pathogenesis of ADO2 (CM2 and CM4), we focused on the differentially expressed genes (DEGs) within these cell subtypes. In the context of CM2, a total of 237 DEGs were identified in the ADO2 mice, including 126 upregulated genes and 111 downregulated genes (Fig. 6a). We performed Gene Ontology (GO) analysis on 111 downregulated genes in CM2 and 145 downregulated genes in CM4. Although we also conducted GO analysis on upregulated genes in ADO2, we did not identify pathways significantly related to osteoclast differentiation. Therefore, we focused our research on the downregulated genes, as they provided more meaningful insights into the mechanisms of osteoclast differentiation. As shown in Fig. 6b and Additional file 1: Fig. S2d, the downregulated DEGs in CM2 were significantly associated with the positive regulation of macrophage activation and interleukin-10 production (GO terms) and the interleukin-17 (IL-17) signaling pathway (Kyoto Encyclopedia of Genes and Genomes (KEGG) terms). For CM4, a total of 390 DEGs were identified in the ADO2 mice, including 245 genes with upregulated expression and 145 genes with downregulated expression (Fig. 6c). As shown in Fig. 6d, the DEGs downregulated in CM2 were significantly associated with in positive regulation of NIK/NF-κB signaling, positive regulation of NF-κB transcription factor activity, positive regulation of macrophage activation and Toll-like receptor binding (GO terms), and in the IL-17 signaling pathway (KEGG terms) (Fig. 6d, e and Additional file 1: Fig. S2e). These results indicated that the DEGs downregulated in both CM2 and CM4 are potentially related to osteoclast differentiation [21, 42].

The analysis of N-linked glycosylation of mononuclear phagocytes in ADO2

Using SUGAR-seq, we found a significant decrease in the surface N-linked glycosylation level of each subtype of mononuclear phagocytes, especially classical monocytes, in ADO2 mice (Figs. 4c and 7a, b). Indeed, all six subtypes

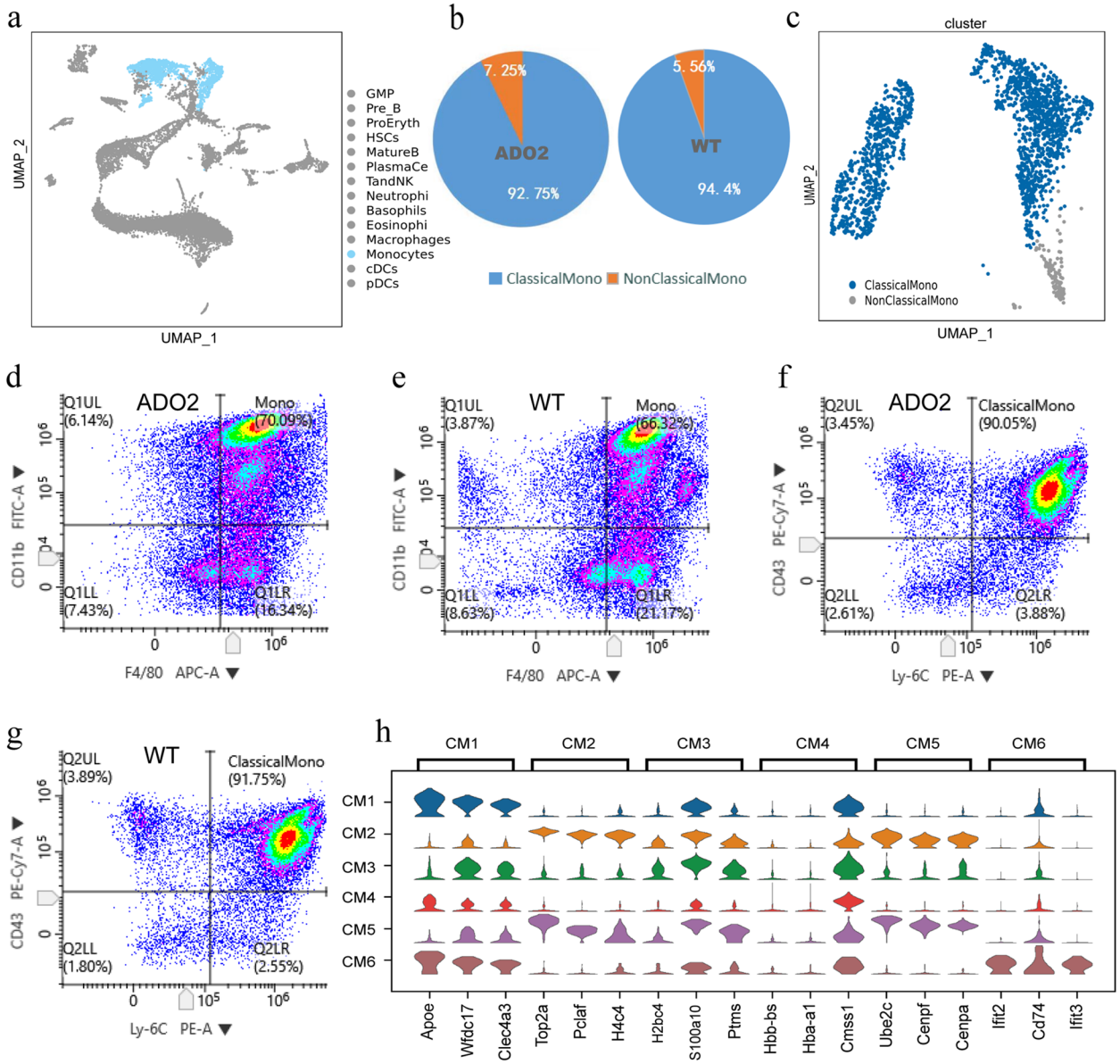

Fig. 5 Characterization of monocyte subpopulations and gene expression in the ADO2 and WT groups. **a** UMAP projection of monocytes within the 14 identified distinct cell clusters, with monocytes labeled in blue. **b** Pie charts illustrating the proportions of classical monocytes and nonclassical monocytes in the WT and ADO2 groups. **c** UMAP projection of classical monocytes within the identified monocyte clusters, with classical monocytes labeled in blue. **d** The visual representation generated through flow cytometry, illustrating the proportion of monocytes within the bone marrow of the ADO2 group. **e** The visual representation generated through flow cytometry, illustrating the proportion of monocytes within the bone marrow of the WT group. **f** The visual representation generated through flow cytometry, illustrating the proportion of classical monocytes within the monocytes in bone marrow of the ADO2 group. **g** The visual representation generated through flow cytometry, illustrating the proportion of classical monocytes within the monocytes in bone marrow of the WT group. **h** Violin plots depicting the expression levels of the top three differentially expressed genes for each of the six subtypes of classical monocytes identified through unsupervised clustering

of classical monocytes had lower N-linked glycosylation levels in the ADO2 mice (Fig. 7b). Through Monocle pseudotime analysis of the six subtypes of classical monocytes, we observed similar differentiation trajectories in the two groups of mice (Fig. 7c). Furthermore, we assessed the differentiation potential of the six subtypes of classical monocytes by integrating CytoTRACE analysis and found that the differentiation potential ordered from high to low was CM2, CM5, CM3, CM1, CM4, and CM6 (Fig. 7d). Based on the Monocle pseudotime and CytoTRACE analysis of the six subtypes of classical monocytes in the ADO2 and WT mice, we obtained

Table 2 Expression of integrin-related genes in classical monocyte subpopulation

Classical monocyte subpopulation	Gene name	Average log2 fold change	P	Gene expression in ADO2	Gene expression in WT
CM1	Itga4	0.337	0.001	1.921	1.729
CM2	Itgb3	0.271	0.039	0.172	0.083
CM3	Itgb7	0.290	0.002	1.523	1.319
CM4	Itgal	0.411	0.001	0.782	0.525
CM5	Itgb3	0.513	0.005	0.248	0.062
CM6	Itgb7	0.374	0.013	1.677	1.485

dynamic N-linked glycosylation for the two groups of mice and found significantly lower N-glycans values in the ADO2 mice in each branch ($P < 0.05$) (Fig. 7e and f).

Our LC–MS/MS analysis also confirmed that numerous proteins exhibited differential N-glycosylation between the two groups of mice. Specifically, we identified 16 proteins with increased abundances of N-glycosylated forms and 66 proteins with decreased abundances of N-glycosylated forms in ADO2 mice. At the level of individual modification sites, there were 18 N-glycosylation modification sites with increased abundance and 86 sites with decreased abundance in ADO2 mice. Strikingly, we observed a general reduction in the abundance of N-glycosylation sites in integrin family proteins, including integrin beta-3 (Itgb3) and integrin beta-7 (Itgb7), in ADO2 mice (Fig. 8a–f). Notably, we found that Itgb7 and Itga3 were abnormally expressed at both the gene and protein levels in CM2 and CM4 cells in ADO2 mice. This finding suggests that the abnormal expression of integrin family genes in ADO2 may affect their glycosylation modifications, potentially impairing the normal functionality of integrins.

LC–MS/MS-based 4D label-free proteomics analysis

Through LC–MS/MS-based 4D label-free proteomics analysis, we identified abnormal expression of the integrin-related protein Itgb7 in ADO2 mouse bone marrow cells, which was found to be elevated compared to WT mice (Table 3). This finding aligns with our single-cell sequencing results, which also revealed upregulation of the integrin-related gene Itgb7 in ADO2 mouse bone marrow cells.

Discussion

In this study, we employed CRISPR/Cas9 technology to establish the first ADO2 mouse model harboring the Clcn7 (R284W) mutation, which corresponds to the CLCN7 (R286W) mutation commonly observed in osteopetrosis patients [43–45]. By utilizing this model, we conducted a comprehensive analysis of the cell types and proportions, transcriptional landscape, and protein N-glycosylation in the bone marrow of ADO2 mice at both the single-cell and cell population levels. We successfully identified a total of 14 cell types in both groups of mice, including GMPs, macrophages, monocytes, and neutrophils, which aligns remarkably well with previously reported research findings [46–50]. This indicates that our single-cell data are reliable. Regarding the bone marrow cell subtypes, we observed a mild increase in the proportion of neutrophils and GMPs in ADO2 mice, while the proportions of monocytes, T and NK cells, mature B cells, cDCs, pDCs, and plasma cells showed a slight reduction. No significant differences were observed

(See figure on next page.)

Fig. 6 Differential gene expression analysis and functional enrichment analysis of CM2 and CM4 in the ADO2 and WT groups. **a** Heatmap displaying the expression levels of the top 20 upregulated genes and top 20 downregulated genes in the CM2 cell cluster between the ADO2 and WT conditions, ranked by the log2 fold change. **b** GO analysis of 111 downregulated genes in CM2. The horizontal coordinate represents the GeneRatio, the vertical coordinates shows the GO term, the color of the circle corresponds to the magnitude of the p.adjust values, and the size of the circle indicates the number of differentially expressed genes. **c** Heatmap displaying the expression levels of the top 20 upregulated genes and top 20 downregulated genes in the CM4 cell cluster between the ADO2 and WT conditions, ranked by the average log-fold change. **d** GO analysis of 145 downregulated genes in CM4. The horizontal coordinate represents the GeneRatio, the vertical coordinate shows the GO term, the color of the circle corresponds to the magnitude of the p.adjust values, and the size of the circle indicates the number of differentially expressed genes. **e** The expression patterns of downregulated genes, which were enriched in the pathways of "positive regulation of macrophage activation," "positive regulation of NIK/NF-κB signaling," "positive regulation of NF-κB transcription factor activity," and "Toll-like receptor binding" in CM2 and CM4 subsets, across all six subtypes of classical monocytes

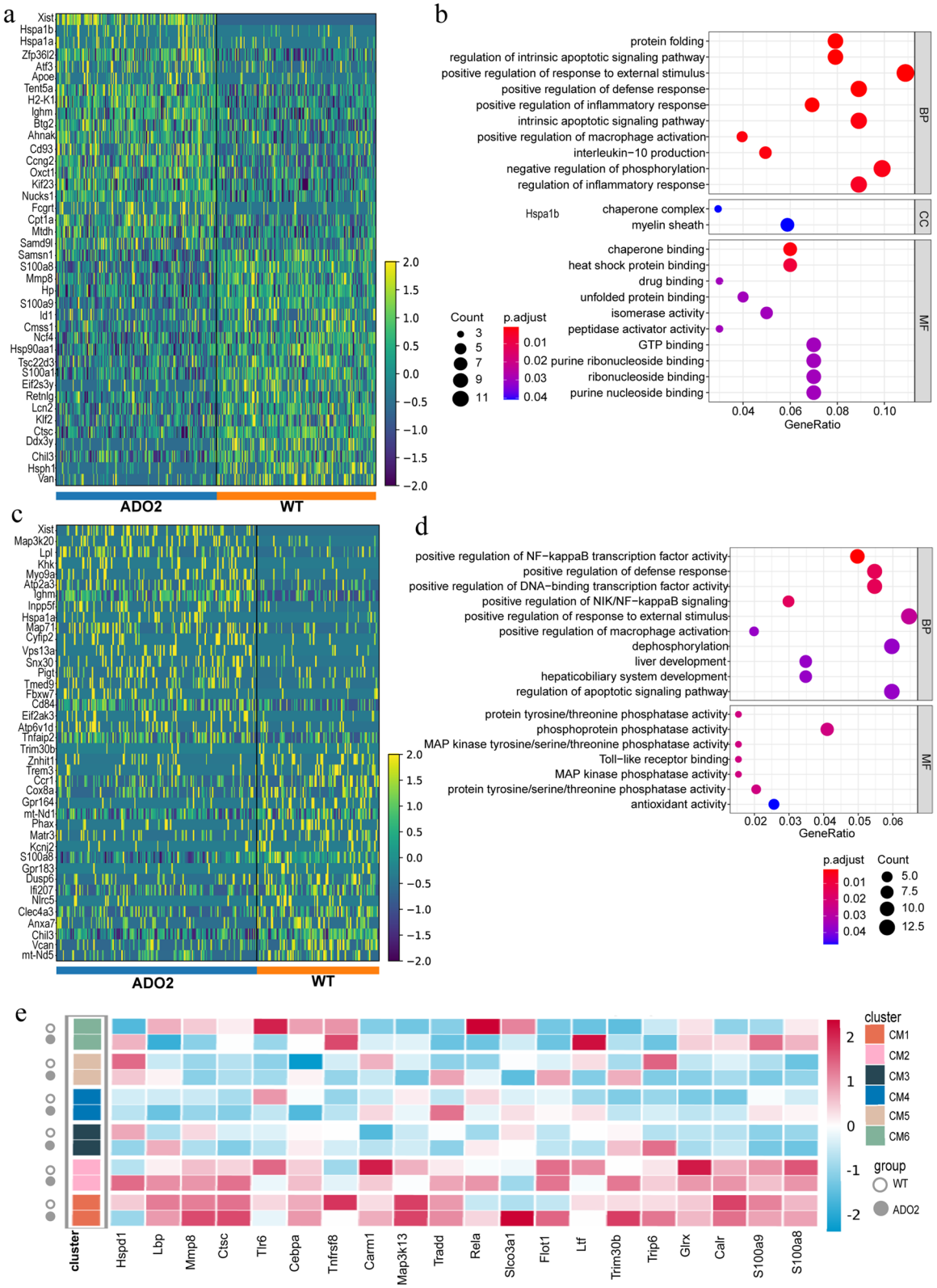

Fig. 6 (See legend on previous page.)

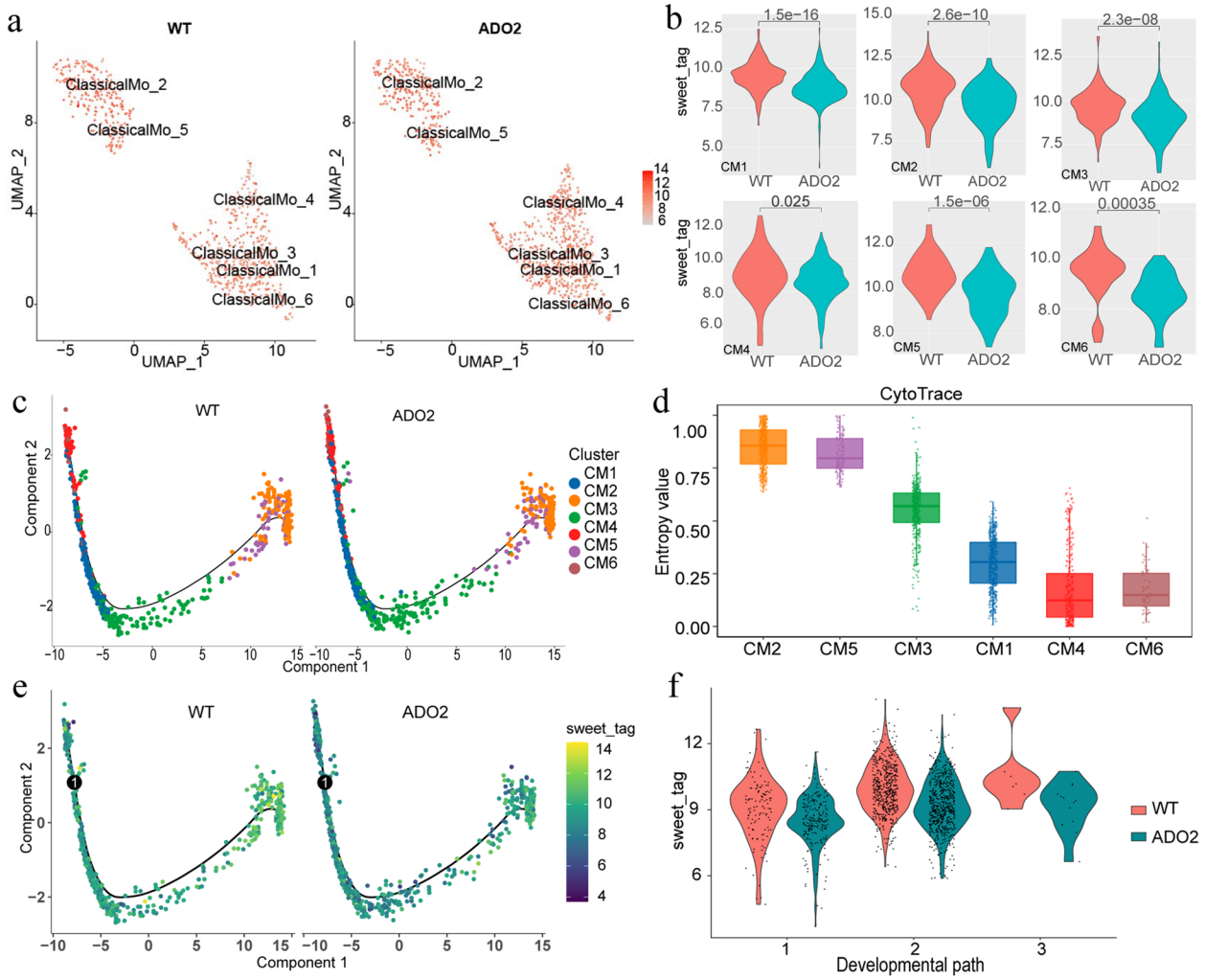

Fig. 7 N-glycans analysis and cellular differentiation in classical monocytes in the ADO2 and WT groups. **a** Featureplot visualization of the N-glycans levels in individual cells in the ADO2 and WT groups, with darker colors indicating higher N-glycans levels. **b** Violin plot comparing the levels of N-glycans in classical monocyte subtypes 1–6 between the ADO2 and WT groups ($P < 0.05$). The average number of glycosylation tags for N-glycans of each subtype are as follows: CM1(ADO2: 8.78389, WT: 9.53651); CM2 (ADO2: 9.66757, WT: 10.4976); CM3 (ADO2: 8.97316, WT: 9.60765); CM4 (ADO2: 8.59505, WT: 8.9693); CM5 (ADO2: 9.69621, WT: 10.6096); CM6 (ADO2: 8.56935, WT: 9.40849). **c** Pseudotime trajectory plot of classical monocyte subtypes in ADO2 disease state compared to normal state. This figure displays the differentiation trajectories of six classical monocyte subtypes inferred through pseudotime analysis. Each node represents a cell subtype, and colors indicate different cell types. The three branches in the plot represent distinct developmental paths, reflecting the dynamic changes and differentiation processes of cells in the ADO2 disease state. Pseudotime increases in the direction of the trajectory, indicating a progression from undifferentiated to mature states from left to right. The trajectory plot is generated based on single-cell RNA sequencing data using the Monocle algorithm for trajectory inference. **d** Boxplot comparing CytoTRACE scores among classical monocyte subtypes 1–6, with higher scores indicating greater differentiation potential. **e** Dynamic changes in N-linked glycosylation between the ADO2 and WT groups based on the Monocle2 pseudotemporal results of the six classical monocyte subtypes. The number 1 inside the black circles represents the nodes identified during trajectory analysis that correspond to different cell states. The differentiation trajectory is divided into three branches. **f** Violin plots illustrating the N-linked glycosylation level of each branch based on the dynamic changes between the ADO2 and WT groups ($P < 0.05$)

in the quantities of other cell types. These findings suggest that Clcn7 (R284W) mutation-associated osteopetrosis does not significantly alter the types of cells present in the bone marrow.

To gain a deeper understanding of how the mutation in this chloride ion channel protein gene affects the metabolism of bone marrow cells, we focused on genes that were differentially expressed in cells with varying quantities and proportions. Our data revealed that these genes are involved in various biological functions, including protein synthesis, mRNA metabolism, cell cycle regulation, cell migration, and adhesion.

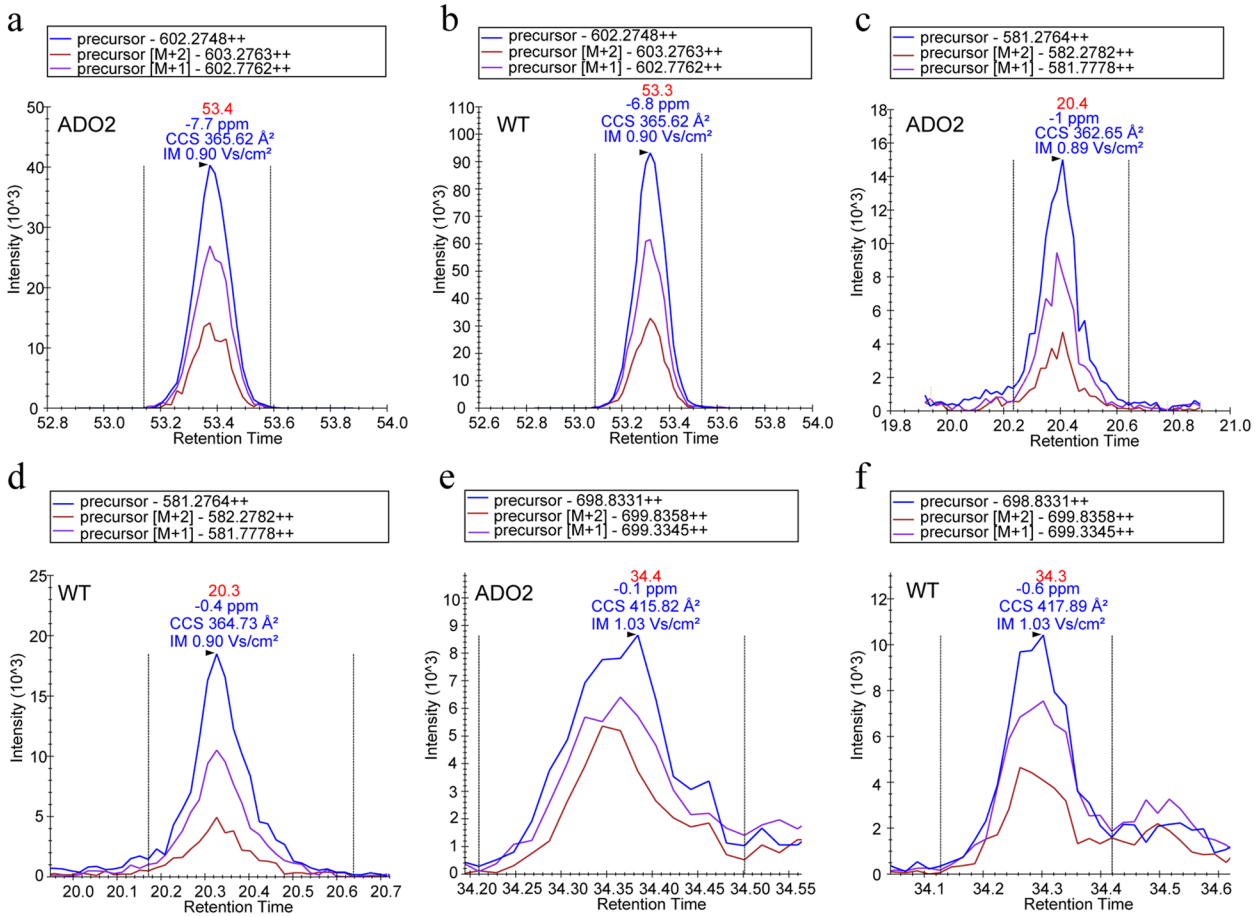

Fig. 8 LC–MS/MS-based 4D Label-Free N-Glycosylation Proteomics Analysis of integrin. **a** Mass Spectrometry Level 1 plot of the itgb3 protein (position: 207) in the ADO2 group. The sequence of itgb3 protein (position: 207) is N(1)ACLPMFGYK and the mass-to-charge ratio (m/z) of it is 602.2748. **b** Mass Spectrometry Level 1 plot of the itgb3 protein (position: 207) in the WT group. **c** Mass Spectrometry Level 1 plot of the itgb7 protein (position: 531) within the ADO2 group. The sequence of the itgb7 protein (position: 531) is APN(1)GTGPLCSGK and the m/z of it is 581.2764. **d** Mass Spectrometry Level 1 plot of the itgb7 protein (position: 531) within the WT group. **e** Mass Spectrometry Level 1 plot of the itgb7 protein (position: 68) within the ADO2 group. The sequence of the itgb7 protein (position:531) is QLN(1)FTASGEAEAR and the m/z of it is 698.8331. **f** Mass Spectrometry Level 1 plot of the itgb7 protein (position:68) within the WT group

Table 3 Expression levels of the Itgb7 protein in the ADO2 and WT groups

Protein	LFQ intensity in ADO2	LFQ intensity in WT	Relative quantification in ADO2	Relative quantification in WT	Fold change
Itgb7	21,408	36,984	0.733251130291821	1.26674886970818	1.72757847533632

The fold change greater than 1.5 indicates a significant upregulation of protein expression

LFQ label-free quantification, *LFQ intensity* intensity values of each protein in different samples, *Relative quantification* relative quantification refers to the ratio of LFQ intensity of a protein to the average intensity of that protein across different samples, *Fold change* the ratio of the relative quantification of a protein in two samples

Furthermore, these genes were found to be enriched in metabolic processes such as glycolysis; gluconeogenesis; the pentose phosphate pathway (related to carbohydrate metabolism); valine, leucine, and isoleucine biosynthesis (related to protein metabolism); lipid metabolism; vitamin B6 metabolism; the citrate cycle; and oxidative phosphorylation (associated with energy metabolism). These findings suggest that metabolic reprogramming in bone marrow cells may be an important pathological characteristic of ADO2 [51, 52].

To understand cell signaling and regulation under the pathological conditions of osteopetrosis, we focused

specifically on analyzing mononuclear phagocytes in ADO2 and control mouse bone marrow. These cells are essential precursors of osteoclasts, which play a critical role in bone resorption and the immune system and are relevant to numerous skeletal diseases [14, 15, 53]. In this study, we employed SUGAR-seq technology to classify and enumerate mononuclear phagocytes, which are closely associated with osteoclast differentiation, in the bone marrow of ADO2 mice. Mononuclear phagocytes include macrophages, classical monocytes, and nonclassical monocytes. Due to the limited counts of macrophages and nonclassical monocytes, we focused on the analysis of classical monocytes and revealed no significant differences in proportion between ADO2 and WT bone marrow. However, upon further subdivision of classical monocytes into six subtypes, we observed significant differences between the CM2 and CM4 subtypes in both groups of mice. This finding suggests that disease-induced changes in cell number may not be apparent at the broad cell type level but can be detected by SUGAR-seq, as it allows the precise identification of cellular subgroups and the detection of subtle intersubgroup differences. Additionally, we observed significantly lower levels of surface protein N-glycosylation in macrophages and monocytes derived from ADO2 mice. Through SUGAR-seq, we unveiled a widespread reduction in cell surface N-linked glycosylation in each classical monocyte subtype, indicating subtle alterations in N-glycans in macrophages, monocytes, and their subgroups in ADO2 mice. These microscale changes in N-glycosylation may impact cellular functions and signaling pathways. Moreover, this further confirms the inherent advantage of SUGAR-seq in exploring disease-induced alterations in cell numbers and microscale changes in surface N-glycans among cellular subgroups. Consequently, this study offers a novel perspective for in-depth investigations into functional disparities among disease-induced cellular subgroups.

Notably, our comprehensive analysis, encompassing both single-cell N-glycosylation and bulk cell N-glycosylation assessments, consistently revealed significantly lower levels of bone marrow cell N-glycosylation in ADO2. Moreover, these changes can be found at the overall population level and in different subtypes of bone marrow cells. Glycosylation, a common protein modification process, involves the attachment of sugar molecules on protein molecules via glycosyltransferases [19, 20]. Glycosylation is regulated by various factors, such as intracellular pH, metal ion concentration, and ion balance [19, 20, 54]. Our results suggest that the observed alterations in N-glycosylation in ADO2 mouse bone marrow cells may be an indirect consequence of specific ion concentration imbalances resulting from gene mutations in chloride ion channel proteins. These imbalances may influence the activity of enzymes involved in N-glycosylation processes, such as peptide N-acetyltransferase activity, ATPase activity, and protein kinase regulator activity [10, 55, 56]. Based on these findings, we postulate that the abnormal N-glycosylation in ADO2 may be closely linked to the abnormal bone metabolism observed in this disorder. This suggests a potential interplay between N-glycosylation alterations and the underlying pathophysiological mechanisms of osteopetrosis.

This study also identified some abnormally expressed glycosylated proteins on the surface of mononuclear phagocytes, including integrin family-related proteins. Integrins consisting of subunits such as alpha (α) and beta (β) subunits play a significant role in modulating the morphology, migration, adhesion, and signal transduction of mononuclear phagocytes during their differentiation into osteoclasts [57, 58]. These effects are mediated through signaling pathways such as TGF-β and NIK/NF-κB, among others [21, 23, 59–61]. Interestingly, we observed that integrin genes including Itgb3 and Itgb7 were abnormally expressed in the various subtypes of classical monocytes in the bone marrow of ADO2, according to our single-cell transcriptomic sequencing data. Furthermore, our mass spectrometry analysis also confirmed that abnormal expression and altered N-glycosylation of integrins with significantly reduced N-glycosylation modifications, such as Itga5 and Itgb7, were found in ADO2 mice. This suggests that the changes in integrin expression and altered N-glycosylation on the surface of mononuclear phagocytes in ADO2 may modify the glycan structure of integrins and affect the regulation of osteoclast differentiation and function [23]. In the context of the subdivision of classical monocytes, our study revealed that Itgb3 gene expression was upregulated in CM4 cells, while the level of N-glycosylation modifications was decreased in this cell subtype. The literature indicates that Itgb3 can activate the NIK/NF-κB signaling pathway via RANK, thereby promoting the fusion of osteoclast precursors into multinucleated osteoclasts and enhancing osteoclast resorptive efficiency during osteoclast differentiation by increasing the surface area of resorption pits. The altered N-glycosylation modifications of Itgb3 observed in CM4 in our study may affect the activation status of Itgb3 and result in reduced activation of the NIK/NF-κB signaling pathway. This observation aligns with our findings of an upregulated NIK/NF-κB signaling pathway and increased NF-κB transcription factor activity in ADO2 mouse bone marrow cells at the single-cell transcriptomic level. Therefore, we speculate that the altered expression and glycan structure modifications of integrins may serve as important

physiological and pathological characteristics contributing to abnormal bone metabolism in osteopetrosis.

LacNAc disaccharide structures are more abundant in N-glycans than O-glycans [62–66]. The SUGAR-seq technology employed in this study is designed for analyzing glycosylation features at the single-cell level, with a focus on N-glycans rather than O-glycans. This preference is due to the method's suitability for detecting the level of N-linked glycosylation. Although O-glycosylation may have significant biological functions in certain contexts, the limitations of our current technology and the critical role of N-glycans in our disease model justify our emphasis on the level of N-linked glycosylation.

In this study, we utilized SUGAR-seq to investigate the N-glycosylation characteristics of the bone marrow microenvironment in the ADO2 mouse model. Understanding the changes in N-glycans during disease progression is crucial for elucidating how glycosylation influences disease mechanisms. However, as noted, the SUGAR-seq technique primarily focuses on single-cell transcriptomic data and surface N-glycosylation levels and does not directly analyze dynamic changes in glycosyltransferases or structural variations in N-glycans.

Despite these technical limitations, our study has revealed significant changes in cell surface N-linked glycosylation under the pathological state of ADO2. These findings provide a unique perspective on the role of the level of N-linked glycosylation in the bone marrow microenvironment and its impact on disease mechanisms. The single-cell data obtained from SUGAR-seq highlight the glycosylation features during disease progression, offering a foundation for future research, even though these findings do not encompass all relevant aspects.

Future research will need to integrate additional methods to further explore the dynamic changes in glycosyltransferases and the structural variations of N-glycans throughout the disease process. Such studies will contribute to a more comprehensive understanding of how these factors influence disease progression and may offer valuable insights for research into ADO2 and similar conditions.

Conclusions

This study confirms that the murine model that we established provides evidence that the human CLCN7 (R286W) mutation is pathogenic in autosomal dominant osteopetrosis (ADO2). Additionally, our single-cell analyses reveal monocyte heterogeneity in ADO2, suggesting that the observed abnormal glycosylation modifications across various subtypes may play crucial roles in the pathogenesis of osteopetrosis.

Methods

Animals

All animal experiments were approved by the Experimental Animal Ethics Committee of Guilin Medical College (Approval No: GLMC-IACUC-2022014, December 5, 2022). In this study, both the experimental and control groups comprised C57BL/6 J mice. All mice used were specific pathogen-free (SPF) grade to ensure a controlled and standardized environment for our experiments. We maintained the ADO2 mutant mouse line by performing self-crosses of F1 heterozygous mice. This approach ensured that the ADO2 heterozygous line was consistently propagated. The wild-type (WT) mice used for generating the F1 cross were from the same C57BL/6 J genetic background as the ADO2 transgenic mice to minimize genetic variation between the experimental and control groups. The WT animals used in our study were littermates of the ADO2 heterozygous mutants, ensuring that both groups shared the same genetic and environmental conditions.

Generation of the ADO2 mouse model and disease characterization

To establish the ADO2 mouse model, we utilized CRISPOR 5.01 (http://crispor.tefor.net) to design the guide RNA (gRNA) sequences, consisting of CRISPR RNA (crRNA) and trans-activating CRISPR RNA (tracRNA), to direct the Cas9 protein for recognition and cleavage of the target DNA sequence in the CRISPR/Cas9 system. The target sequence of specific gRNA was 5′-TCCGCAGAGATACAGAGAAGCGG-3′. Additionally, a donor oligo sequence was designed to introduce the p.R284W (CGG to TGG) mutation along with two synonymous mutations (p.R278 = (CGC to AGG) and p.K283 = (AAG to AAA)) [67]. The donor oligo sequence was 5′-AGCCCTCGCAGGCCCTCAAACCCCTCTCTTTCAGATTTGAATATTTCAGGAGGATACAGAAATGGGATTGTCAGCTGGAGCTGCAGCTGGTATCTGCTGCATTTAGCCCCCCTGTGGG-3′.

Next, the crRNA (Genscript Biotech) was synthesized and combined with the tracRNA (IDT) to form the gRNA. The Cas9 protein (Abcam) was assembled with gRNA to form a ribonucleoprotein (RNP) complex, known as the Cas9-gRNA complex. This complex, along with the donor oligo, was microinjected into the nuclei of mouse zygotes under an inverted microscope.

The zygotes were then transferred to M16 medium (Sigma) and placed in a 37 °C, 5% CO_2 incubator for 0.5–1 h before being transplanted into the oviducts of

surrogate mothers. The surrogate mothers gave birth approximately 20 days after successful embryo transfer. To identify transgenic mice (F0), genomic DNA was extracted from mouse tails using the TaKaRa MiniBEST Universal Genomic DNA Extraction kit (Ver.5.0 Code No.9725). Subsequently, the extracted mouse DNA was amplified using the following primer pair: F: 5′-AAA ATGCTCCCTGCTTGATTATCTC-3′, R: 5′-TTCCTA AGGGATGGAGAAGTTGAT-3′.

The polymerase chain reaction (PCR) products were evaluated by agarose gel electrophoresis, the PCR products were collected for sequencing verification, and Chromas software (Version 2.5.1) was used to process the DNA sequence data.

Finally, F0 mice were bred with nontransgenic mice to produce F1 mice. Offspring of F0 that inherit the integrated target gene have a 50% chance of transmitting the mutation through the germline. The process of generating CRISPR/Cas9 point mutation mice is illustrated in Fig. 1a.

Hematoxylin and eosin staining of femoral sections in ADO2 mice

For histological analysis, femoral sections from 7-week-old ADO2 and WT mice were used. The mice were first anesthetized and euthanized, followed by dissection and disinfection of the femur tissue. The extracted femur tissue was fixed in paraformaldehyde (4%, Solarbio). After fixation, the tissue was dehydrated using different concentrations of ethanol, soaked in xylene (Sangon Biotech), and embedded in paraffin, followed by sectioning.

Consecutive sections were then obtained from the tissue and subjected to staining with hematoxylin (MXB Biotechnologies) and subsequently with eosin (ZSGB-BIO). Subsequently, the femoral sections of the mice were observed and analyzed under a microscope to gather information about their histological structure. Then, multiple measurements were taken at different locations along the femoral diaphysis, including both the thickest and thinnest regions, and we calculated the mean and standard deviation for each group.

X-ray and ^{18}F-NaF PET/CT imaging for bone metabolism assessment

The PET/CT imaging technique employed in our study utilizes ^{18}F-fluoride (^{18}F-NaF) as a tracer. This tracer accumulates in bone tissue in proportion to bone blood flow, bone metabolism, and levels of osteoblastic and osteoclastic activity. Specifically, increased ^{18}F-NaF uptake reflects higher bone metabolism and more active bone remodeling.

Comparative X-ray analysis of 7-week-old heterozygous mice and wild-type mice was conducted using the "X-RAY" module of the IVIS Lumin XRMS Series III In Vivo Imaging Device (Perkin Elmer).

For ^{18}F-NaF PET/CT imaging, the mice were anesthetized with isoflurane gas, and 200 μCi (0.2 mL) of ^{18}F-NaF labeled with the Allinone module was intravenously injected via the tail vein [68, 69]. There were 5 mice (10 weeks old) each in the ADO2 group and the WT group. Following injection, the mice were returned to the animal cage for recovery and imaging. Five minutes before imaging, the mice were anesthetized again and placed in a submillimeter micro PET/CT (MadicLAB) animal chamber. PET and CT acquisition started 45 ± 5 min after injection, with the tube voltage set at 80 kV and tube current at 0.6 mA. The PET reconstruction p meters were set to an accuracy of 150 μm.

PET/CT fused images were processed using PMOD 4.3 software. We processed the PET/CT images using fusion imaging techniques to delineate the region of interest (ROI) in the left femur of the mice. We then measured and calculated the standard uptake value (SUV) and derived the maximum standard uptake value (SUVmax) within this ROI. The formula for calculating SUV is as follows:

A higher SUVmax indicates greater bone metabolism. This method provides a reliable measure of bone metabolic activity and allows for comparison between ADO2 and WT mice.

Bone marrow cell samples

After anesthetization using isoflurane, three ADO2 and three WT mice were euthanized. Subsequently, the femurs of the mice were dissected, and bone marrow cells were extracted. The obtained cell suspension was then filtered through a 200-μm cell filter. Next, GEXSCOPE® Red Blood Cell Lysis Buffer (RCLB, Singleron) was added to the mixture to remove red blood cells. The samples were then centrifuged at 300 × *g* and 4 °C for 5 min to discard the supernatant, followed by gentle resuspension in PBS. The bone marrow cells from the femurs were allocated for SUGAR-seq analysis and LC–MS/MS-based 4D Label-Free proteomics and N-Glycosylation proteomics analysis. The samples used for flow cytometry analysis were taken from another three wild-type mice and three mice heterozygous for the mutation using the same protocol.

SUGAR-seq analysis

In our study, we employed SUGAR-seq technology to perform the analysis of the RNA expression profiles and the cell surface features of N-linked glycosylation of

ADO2 mouse single bone marrow cells. The workflow of SUGAR-seq, as illustrated in Fig. 2a, enabled us to comprehensively investigate the gene expression and N-glycans profiles at the single-cell level.

Cell preparation and viability assessment

Following the collection of the cell suspension, centrifugation was performed at 500×*g* for 5 min. The resulting pellet was resuspended in staining buffer and stained with Trypan blue to assess cell dissociation efficiency and viability (at least 85%).

Labeling of N-linked glycosylation on the surface of bone marrow cells in ADO2 mice

The ProMoSCOPE™ Single Cell Glycosylation Detection Kit (Singleron Biotechnologies) was used to label cell surface glycosylation, with a primary focus on detecting N-linked glycosylation, following the manufacturer's instructions. This kit enable accurate quantification of cell surface glycosylation level, with a primary focus on detecting N-linked glycosylation, together with gene expression profiles at the single-cell level. In summary, the two groups of bone marrow cells and the fucose residues carrying a tag consisting of a PCR handle, a known sequence, and a polyA sequence were used to label cell surface glycosylation, with a primary focus on detecting N-linked glycosylation. This is accomplished through a chemoenzymatic method in which the ProMoSCOPE tag forms a covalent bond with N-Acetyllactosamine (LacNAc) on the cell surface by employing a recombinant *Helicobacter pylori* α1,3-fucosyltransferase (1,3-FucT) characterized by its exceptional ability to accept donor substrates, enabling the transfer of a C-6 ssDNA-tagged fucose residue to the carbon atom 3 of GlcNAc within the LacNAc disaccharide [17]. After washing three times to remove excess labels, the cells were resuspended in phosphate-buffered saline (PBS) at an appropriate concentration, and subsequent operations were performed according to the manual.

Reverse transcription, amplification, and library construction

The Singleron Matrix® Single Cell Processing System was used to load single-cell suspensions (2×105 cells/mL) in PBS (HyClone) onto a microwell chip. After the isolation of individual cells, lysis and barcoding, the barcoding beads, which have a PCR handle, a known sequence, and a polyA sequence on their surface, were collected for subsequent reverse transcription and PCR amplification. These barcoded beads capture the mRNA molecules of each single cell, assigning a unique barcode to each, thereby enabling the independent analysis of gene expression from individual cells within a multicellular sample. The amplified cDNA was then fragmented, followed by adapter ligation and another round of PCR amplification. The resulting amplified cDNA libraries were constructed for the Illumina sequencing platform. The ProMoSCOPE products were further amplified by PCR to generate sequencing libraries suitable for Illumina sequencing. Individual libraries were diluted to 4 nM, pooled together, and sequenced on the Illumina NovaSeq 6000 platform using the 150 bp paired-end strategy.

SUGAR-seq data processing

Barcodes and UMIs were extracted from R1 reads and corrected. Adapter sequences and poly-A tails were trimmed from R2 reads using Cutadapt v3.7. After preprocessing, the R2 reads were mapped to the GRCm38 (mm10) transcriptome using STAR v2.6.1. Subsequently, uniquely mapped reads were categorized into exons using FeatureCounts(v2.0.1). To create the gene expression matrix for subsequent analysis, reads with identical cell barcodes, UMIs, and genes were grouped together.

Single-cell ProMoSCOPE library analysis

To identify the N-glycans positions, the 15-bp tag sequence was extracted from the R2 reads and compared to the known glycosylation tag sequence. Tags with a Hamming distance of less than 2 were classified as valid tags. The count of tag Unique Molecular Identifiers (UMI) present within each cell barcode was tallied to produce a single-cell glycosylation UMI expression matrix.

Subsequently, we performed quality control, dimension reduction, clustering, and bioinformatics analysis on the obtained data. Detailed methods, including quality control, dimension reduction, and clustering; batch effect removal; differentially expressed gene analysis; pathway enrichment; cell type annotation; subtyping of major cell types; filtering of cell doublets; pseudotime trajectory analysis; N-glycan degree data processing and mapping; and scMetabolism analysis, can be found in the Supplementary Information File (SI) File.

Flow cytometry analysis

For the 6 bone marrow cell suspensions collected from three wild-type mice and three heterozygous mutant mice, 100 μL of the suspension was transferred to each flow tube. Then, 5 μL of CD45 PerCP/Cyanine5.5 (URIT), CD11b FITC (URIT), F4/80 APC (URIT), Ly6C PE (URIT), CD43 PE-Cy7 (URIT), and Ly6G APC-Cy7 (URIT) were added to each tube and thoroughly mixed and were incubated in the dark for 20 min. Following the addition of red blood cell lysis buffer (URIT) to lyse the

red blood cells in each sample, the samples were centrifuged at 350 *g* for 5 min, and the supernatant was discarded. After washing and resuspending the cells with PBS, cell analysis was performed using a flow cytometer (URIT BF-700, URIT Medical Electronic Co., Ltd).

LC–MS/MS-based 4D label-free proteomics and N-glycosylation proteomics analysis

We conducted LC–MS/MS-based 4D label-free N-glycosylation proteomics analysis and LC–MS/MS-based 4D label-free proteomics analysis on ADO2 mouse bone marrow cells, with detailed methods found in the Additional file 3 [70–75].

Methods of statistical analysis

We conducted statistical analyses on the data obtained from ^{18}F-NaF PET/CT imaging and flow cytometry using the *t* test in GraphPad Prism Software (version 9.0). For the SUGAR-seq analysis, we used the Wilcoxon test to analyze paired data for the level of N-linked glycosylation and applied the chi-square test using SPSS (version 25.0) to investigate the proportions of annotated cell types in the overall population. $P < 0.05$ indicated statistical significance.

Abbreviations

ADO2	Autosomal dominant osteopetrosis type 2
BMCs	Bone marrow cells
cDCs	Conventional dendritic cells
DEGs	Differentially expressed genes
ClassicalMono	Classical monocytes
CM1	ClassicaMo_1
CM2	ClassicaMo_2
CM3	ClassicaMo_3
CM4	ClassicaMo_4
CM5	ClassicaMo_5
CM6	ClassicaMo_6
CRISPR/Cas9	Clustered Regularly Interspaced Short Palindromic Repeats / CRISPR-associated protein 9
GMP	Granulocyte-monocyte progenitor cells
GO	Gene Ontology
HE	Hematoxylin and eosin
HSCs	Hematopoietic stem cells
IL-17	Interleukin-17
Itgb3	Integrin beta-3
Itgb7	Integrin beta-7
KEGG	Kyoto Encyclopedia of Genes and Genomes
LacNAc	N-Acetyllactosamine
LFQ	Label-free quantification
MatureB	Mature B cells
M-CSF	Macrophage-colony stimulating factor
MPS	Mononuclear phagocyte system
NIK/NF-κB	NF-κB-inducing kinase / Nuclear Factor-kappa B
PET/CT	Positron emission tomography/ computed tomography
NonClassicalMono	Nonclassical monocytes
pDCs	Plasmacytoid dendritic cells
PlasmaCells	Plasma cells
Pre-B	Precursor B cell
ProEryth	Erythroid progenitor cells
RANKL	Receptor activator of nuclear factor kappa B ligand
ROI	Region of interest
SUGAR-seq	SUrface-protein Glycan And RNA-sequencing
SUVmax	Maximum standardized uptake value
TandNK	T and NK cells
UMAP	Uniform manifold approximation and projection

Supplementary Information

The online version contains supplementary material available at https://doi.org/10.1186/s12915-025-02193-z.

Additional File 1: Figures S1-S3. Fig S1-[Alterations in cellular metabolic activity, as revealed by scMetabolism analysis.]. Fig S2-[Gene expression and enrichment analysis of macrophages, marker genes for monocyte subtypes, and functional enrichment analysis of CM2 and CM4.].

Additional File 2: Table S1-S6. Table S1-[Comparison of SUVmax Values among Groups of ADO2 and WT]. Table S2-[Comparison of the proportion of neutrophils in bone marrow cells between the ADO2 and WT groups by flow cytometry]. Table S3-[Comparison of ClassicalMono and NonClassicalMono proportions between WT and ADO2 groups using the chi-square test]. Table S4-[Comparison of the proportion of monocyte in bone marrow cells between the ADO2 and WT groups by flow cytometry]. Table S5-[Comparison of the proportion of classical monocyte in bone marrow cells between the ADO2 and WT groups by flow cytometry]. Table S6-[Comparison of cell proportions of the six subtypes of ClassicalMono between the WT and ADO2 groups using the chi-square test].

Additional File 3. Detailed methods of LC–MS/MS-based 4D Label-Free N-Glycosylation Proteomics Analysis and LC–MS/MS-based 4D Label-Free Proteomics Analysison ADO2 mouse bone marrow cells.

Acknowledgements

This research was founded by National Natural Science Foundation of China (Grant NO. 82060393) and Guangxi Natural Science Foundation (NO. 2020GXNSFAA159124). We would like to express our gratitude to Honghao Yu, Ge Peng, and Xinyun Huang for their valuable assistance to this paper.

Authors' contributions

Conceptualization: MO, YS. Data curation: YS, LH, LZ. Formal analysis: YS, LH. Funding acquisition: MO. Investigation: YS, LH, CM, CP, GC, SL. Methodology: MO, YS. Project administration: MO. Resources: MO. Software: YS, LH, LZ. Supervision: XH. Validation: XH. Visualization: YS, LZ. Roles/Writing—original draft: YS. Writing—review & editing: MO, YS. All authors read and approved the final manuscript.

Funding

This research was founded by National Natural Science Foundation of China (No. 82060393) and Guangxi Natural Science Foundation (No. 2024GXNSFAA010392).

Data availability

The SUGAR-seq data generated in this study have already been deposited in NCBI under the BioProject accession PRJNA1219686 (https://www.ncbi.nlm.nih.gov/bioproject/PRJNA1219686) [76]. Similarly, the MS/MS-based 4D Label-Free N-Glycosylation Proteomics Analysis data have been deposited to the ProteomeXchange Consortium via the iProX partner repository with the dataset identifier PXD060501 (https://www.iprox.cn/page/project.html?id=IPX0011013000) [77]. The LC–MS/MS-based 4D Label-Free Proteomics Analysis data have been deposited to the ProteomeXchange Consortium via the iProX partner repository with the dataset identifier PXD060536 (https://www.iprox.cn/page/project.html?id=IPX0011019000) [78].

Declarations

Ethics approval and consent to participate

The experiments approved by the Experimental Animal Ethics Committee of Guilin Medical College (Approval No: GLMC-IACUC-2022014, December 5, 2022).

Consent for publication
Not applicable.

Competing interests
The authors declare that they have no competing interests.

Author details
[1]Laboratory Center, Guangxi Key Laboratory of Metabolic Reprogramming and Intelligent Medical Engineering for Chronic Diseases, The Second Affiliated Hospital of Guilin Medical University, Guilin 541199, China. [2]Key Laboratory of Medical Biotechnology and Translational Medicine (Guilin Medical University), Education Department of Guangxi Zhuang Autonomous Region, Guilin 541199, China. [3]The Department of Nuclear Medicine, Affiliated Hospital of Guilin Medical University, Guilin 541001, China.

Received: 15 February 2024 Accepted: 14 March 2025
Published online: 31 March 2025

References

1. Nguyen A, Miller WP, Gupta A, Lund TC, Schiferl D, Lam LSK, et al. Open-Label Pilot Study of Interferon Gamma-1b in Patients With Non-Infantile Osteopetrosis. JBMR Plus. 2022;6(3): e10597.
2. Superti-Furga A, Unger S. Nosology and classification of genetic skeletal disorders: 2006 revision. Am J Med Genet A. 2007;143A(1):1–18.
3. Tolar J, Teitelbaum SL, Orchard PJ. Osteopetrosis. N Engl J Med. 2004;351(27):2839–49.
4. Chawla A, Kwek EBK. Fractures in patients with osteopetrosis, insights from a single institution. Int Orthop. 2019;43(6):1297–302.
5. Tu Y, Liu FX, Jia HL, Yang JJ, Lv XL, Li C, et al. The Treatment of Subtrochanteric Fracture with Reversed Contralateral Distal Femoral Locking Compression Plate (DF-LCP) Using a Progressive and Intermittent Drilling Procedure in Three Osteopetrosis Patients. Orthop Surg. 2022;14(2):254–63.
6. Cao W, Wei W, Yu G, Wu Q, Qin M. Comparison of Optic Canal Diameter in Children With Malignant Infantile Osteopetrosis and Normal Children and the Effects of Hematopoietic Stem Cell Transplantation on the Optic Canal Diameter. J Pediatr Ophthalmol Strabismus. 2019;56(1):35–42.
7. Li C, Shangguan Y, Zhu P, Dai W, Tang D, Ou M, et al. Multiomics landscape of the autosomal dominant osteopetrosis type II disease-specific induced pluripotent stem cells. Hereditas. 2021;158(1):40.
8. Li D, Ou M, Zhang W, Luo Q, Cai W, Mo C, et al. CRISPR/Cas9-Mediated Gene Correction in Osteopetrosis Patient-Derived iPSCs. Front Biosci (Landmark Ed). 2023;28(6):131.
9. Ou M, Li C, Tang D, Xue W, Xu Y, Zhu P, et al. Genotyping, generation and proteomic profiling of the first human autosomal dominant osteopetrosis type II-specific induced pluripotent stem cells. Stem Cell Res Ther. 2019;10(1):251.
10. Stauber T, Wartosch L, Vishnolia S, Schulz A, Kornak U. CLCN7, a gene shared by autosomal recessive and autosomal dominant osteopetrosis. Bone. 2023;168: 116639.
11. Sui W, Ou M, Liang J, Ding M, Chen J, Liu W, et al. Rapid gene identification in a Chinese osteopetrosis family by whole exome sequencing. Gene. 2013;516(2):311–5.
12. Polgreen LE, Imel EA, Econs MJ. Autosomal dominant osteopetrosis. Bone. 2023;170: 116723.
13. Gordon S, Plüddemann A. The Mononuclear Phagocytic System. Generation of Diversity Front Immunol. 2019;10:1893.
14. Roth P, Dominguez MG, Stanley ER. The effects of colony-stimulating factor-1 on the distribution of mononuclear phagocytes in the developing osteopetrotic mouse. Blood. 1998;91(10):3773–83.
15. Udagawa N, Takahashi N, Akatsu T, Tanaka H, Sasaki T, Nishihara T, et al. Origin of osteoclasts: mature monocytes and macrophages are capable of differentiating into osteoclasts under a suitable microenvironment prepared by bone marrow-derived stromal cells. Proc Natl Acad Sci U S A. 1990;87(18):7260–4.
16. Illiano A, Pinto G, Melchiorre C, Carpentieri A, Faraco V, Amoresano A. Protein Glycosylation Investigated by Mass Spectrometry: An Overview. Cells. 2020;9(9):1986.
17. Moremen KW, Tiemeyer M, Nairn AV. Vertebrate protein glycosylation: diversity, synthesis and function. Nat Rev Mol Cell Biol. 2012;13(7):448–62.
18. Ohtsubo K, Marth JD. Glycosylation in cellular mechanisms of health and disease. Cell. 2006;126(5):855–67.
19. Reily C, Stewart TJ, Renfrow MB, Novak J. Glycosylation in health and disease. Nat Rev Nephrol. 2019;15(6):346–66.
20. Schjoldager KT, Narimatsu Y, Joshi HJ, Clausen H. Global view of human protein glycosylation pathways and functions. Nat Rev Mol Cell Biol. 2020;21(12):729–49.
21. Asai K, Funaba M, Murakami M. Enhancement of RANKL-induced MITF-E expression and osteoclastogenesis by TGF-β. Cell Biochem Funct. 2014;32(5):401–9.
22. Feng G, Zhou Y, Yan J, Wang Z, Yang Y, Zhao W, et al. Proteomic and N-glycoproteomic analyses of total subchondral bone protein in patients with primary knee osteoarthritis. J Proteomics. 2023;280: 104896.
23. Kim HH, Chung WJ, Lee SW, Chung PJ, You JW, Kwon HJ, et al. Association of sustained ERK activity with integrin beta3 induction during receptor activator of nuclear factor kappaB ligand (RANKL)-directed osteoclast differentiation. Exp Cell Res. 2003;289(2):368–77.
24. Takayanagi H, Iizuka H, Juji T, Nakagawa T, Yamamoto A, Miyazaki T, et al. Involvement of receptor activator of nuclear factor kappaB ligand/osteoclast differentiation factor in osteoclastogenesis from synoviocytes in rheumatoid arthritis. Arthritis Rheum. 2000;43(2):259–69.
25. Kearney CJ, Vervoort SJ, Ramsbottom KM, Todorovski I, Lelliott EJ, Zethoven M, et al. SUGAR-seq enables simultaneous detection of glycans, epitopes, and the transcriptome in single cells. Sci Adv. 2021;7(8):eabe3610.
26. Odaka H, Ozaki H, Tateno H. scGR-seq: Integrated analysis of glycan and RNA in single cells. STAR Protoc. 2022;3(1): 101179.
27. Yu W, Zhao X, Jalloh AS, Li Y, Zhao Y, Dinner B, et al. Chemoenzymatic Measurement of LacNAc in Single-Cell Multiomics Reveals It as a Cell-Surface Indicator of Glycolytic Activity of CD8+ T Cells. J Am Chem Soc. 2023;145(23):12701–16.
28. Zhang Y, Warden AR, Ahmad KZ, Liu Y, He X, Zheng M, et al. Single-Cell Microwell Platform Reveals Circulating Neural Cells as a Clinical Indicator for Patients with Blood-Brain Barrier Breakdown. Res (Wash D C). 2021;2021:9873545.
29. Yan R, Zhang H, Ma Y, Lin R, Zhou B, Zhang T, et al. Discovery of Muscle-Tendon Progenitor Subpopulation in Human Myotendinous Junction at Single-Cell Resolution. Res (Wash D C). 2022;2022:9760390.
30. McDonald MM, Kim AS, Mulholland BS, Rauner M. New Insights Into Osteoclast Biology. JBMR Plus. 2021;5(9): e10539.
31. Vuoti E, Lehenkari P, Tuukkanen J, Glumoff V, Kylmäoja E. Osteoclastogenesis of human peripheral blood, bone marrow, and cord blood monocytes. Sci Rep. 2023;13(1):3763.
32. Yahara Y, Nguyen T, Ishikawa K, Kamei K, Alman BA. The origins and roles of osteoclasts in bone development, homeostasis and repair. Development. 2022;149(8):dev199908.
33. Bao J, Yan Y, Zuo D, Zhuo Z, Sun T, Lin H, et al. Iron metabolism and ferroptosis in diabetic bone loss: from mechanism to therapy. Front Nutr. 2023;10:1178573.
34. Da W, Tao L, Zhu Y. The Role of Osteoclast Energy Metabolism in the Occurrence and Development of Osteoporosis. Front Endocrinol. 2021;12: 675385.
35. Kim Y, Lee Y, Lee MN, Nah J, Yun N, Wu D, Pae M. Time-restricted feeding reduces monocyte production by controlling hematopoietic stem and progenitor cells in the bone marrow during obesity. Front Immunol. 2022;13:1054875.
36. Martyniak K, Wei F, Ballesteros A, Meckmongkol T, Calder A, Gilbertson T, et al. Do polyunsaturated fatty acids protect against bone loss in our aging and osteoporotic population? Bone. 2021;143: 115736.
37. Perić Kačarević Ž, Rider P, Alkildani S, Retnasingh S, Pejakić M, Schnettler R, et al. An introduction to bone tissue engineering. Int J Artif Organs. 2020;43(2):69–86.
38. Boeyens JC, Deepak V, Chua WH, Kruger MC, Joubert AM, Coetzee M. Effects of ω3- and ω6-polyunsaturated fatty acids on RANKL-induced osteoclast differentiation of RAW264.7 cells: a comparative in vitro study. Nutrients. 2014;6(7):2584–601.
39. Coxon FP, Rogers MJ. The role of prenylated small GTP-binding proteins in the regulation of osteoclast function. Calcif Tissue Int. 2003;72(1):80–4.
40. Oh SR, Sul OJ, Kim YY, Kim HJ, Yu R, Suh JH, Choi HS. Saturated fatty acids enhance osteoclast survival. J Lipid Res. 2010;51(5):892–9.

41. Roy M, Roux S. Rab GTPases in Osteoclastic Bone Resorption and Autophagy. Int J Mol Sci. 2020;21(20):7655.
42. Kawai T, Akira S. Signaling to NF-kappaB by Toll-like receptors. Trends Mol Med. 2007;13(11):460–9.
43. Hsu PD, Lander ES, Zhang F. Development and applications of CRISPR-Cas9 for genome engineering. Cell. 2014;157(6):1262–78.
44. Redman M, King A, Watson C, King D. What is CRISPR/Cas9? Arch Dis Child Educ Pract Ed. 2016;101(4):213–5.
45. Yin H, Xue W, Chen S, Bogorad RL, Benedetti E, Grompe M, et al. Genome editing with Cas9 in adult mice corrects a disease mutation and phenotype. Nat Biotechnol. 2014;32(6):551–3.
46. Boisset JC, Vivié J, Grün D, Muraro MJ, Lyubimova A, van Oudenaarden A. Mapping the physical network of cellular interactions. Nat Methods. 2018;15(7):547–53.
47. Rodriguez-Fraticelli AE, Wolock SL, Weinreb CS, Panero R, Patel SH, Jankovic M, et al. Clonal analysis of lineage fate in native haematopoiesis. Nature. 2018;553(7687):212–6.
48. Stumpf PS, Du X, Imanishi H, Kunisaki Y, Semba Y, Noble T, et al. Transfer learning efficiently maps bone marrow cell types from mouse to human using single-cell RNA sequencing. Commun Biol. 2020;3(1):736.
49. Yao RQ, Li ZX, Wang LX, Li YX, Zheng LY, Dong N, et al. Single-cell transcriptome profiling of the immune space-time landscape reveals dendritic cell regulatory program in polymicrobial sepsis. Theranostics. 2022;12(10):4606–28.
50. Zhong J, Mao X, Li H, Shen G, Cao X, He N, et al. Single-cell RNA sequencing analysis reveals the relationship of bone marrow and osteopenia in STZ-induced type 1 diabetic mice. J Adv Res. 2022;41:145–58.
51. Sung JY, Cheong JH. Pan-Cancer Analysis Reveals Distinct Metabolic Reprogramming in Different Epithelial-Mesenchymal Transition Activity States. Cancers (Basel). 2021;13(8):1778.
52. Yoshida GJ. Metabolic reprogramming: the emerging concept and associated therapeutic strategies. J Exp Clin Cancer Res. 2015;34:111.
53. Anwar A, Sapra L, Gupta N, Ojha RP, Verma B, Srivastava RK. Fine-tuning osteoclastogenesis: An insight into the cellular and molecular regulation of osteoclastogenesis. J Cell Physiol. 2023;238(7):1431–64.
54. Swietach P. What is pH regulation, and why do cancer cells need it? Cancer Metastasis Rev. 2019;38(1–2):5–15.
55. Penna S, Villa A, Capo V. Autosomal recessive osteopetrosis: mechanisms and treatments. Dis Model Mech. 2021;14(5):dmm048940.
56. Zifarelli G. The Role of the Lysosomal Cl-/H+ Antiporter ClC-7 in Osteopetrosis and Neurodegeneration. Cells. 2022;11(3):366.
57. Faccio R, Takeshita S, Zallone A, Ross FP, Teitelbaum SL. c-Fms and the alphavbeta3 integrin collaborate during osteoclast differentiation. J Clin Invest. 2003;111(5):749–58.
58. Mezu-Ndubuisi OJ, Maheshwari A. The role of integrins in inflammation and angiogenesis. Pediatr Res. 2021;89(7):1619–26.
59. Bellis SL. Variant glycosylation: an underappreciated regulatory mechanism for beta1 integrins. Biochim Biophys Acta. 2004;1663(1–2):52–60.
60. Janik ME, Lityńska A, Vereecken P. Cell migration-the role of integrin glycosylation. Biochim Biophys Acta. 2010;1800(6):545–55.
61. Marsico G, Russo L, Quondamatteo F, Pandit A. Glycosylation and Integrin Regulation in Cancer. Trends Cancer. 2018;4(8):537–52.
62. Yu W, Zhao X, Jalloh AS, Li Y, Zhao Y, Dinner B, et al. Chemoenzymatic measurement of LacNAc in single-cell multiomics reveals it as a cell-surface indicator of glycolytic activity of CD8+ T cells. J Am Chem Soc. 2023;145(23):12701–16.
63. Ujita M, Fukuda M. Regulation of poly-N-acetyllactosamine biosynthesis in O-glycans. Trends Glycosci Glycotechnol. 2001;13(70):177–91.
64. Nonaka M, Fukuda M. Expression and function of poly-N-acetyllactosamine type glycans in cancer. In: Furukawa K, Fukuda M, editors. Glycosignals in cancer: mechanisms of malignant phenotypes. Tokyo: Springer; 2016. p. 141–61. https://link.springer.com/book/10.1007/978-4-431-55939-9#page=143.
65. Sauerzapfe B, Křenek K, Schmiedel J, Wakarchuk WW, Pelantová H, Křen V, Elling L. Chemo-enzymatic synthesis of poly-N-acetyllactosamine (poly-LacNAc) structures and their characterization for CGL2-galectin-mediated binding of ECM glycoproteins to biomaterial surfaces. Glycoconj J. 2009;26:141–59.
66. Viinikangas T, Khosrowabadi E, Kellokumpu S. N-glycan biosynthesis: basic principles and factors affecting its outcome. Antibody Glycosyl. 2021;112:237–57.
67. Concordet JP, Haeussler M. CRISPOR: intuitive guide selection for CRISPR/Cas9 genome editing experiments and screens. Nucleic Acids Res. 2018;46(W1):W242–5.
68. MacKay JW, Watkins L, Gold G, Kogan F. [18F]NaF PET-MRI provides direct in-vivo evidence of the association between bone metabolic activity and adjacent synovitis in knee osteoarthritis: a cross-sectional study. Osteoarthritis Cartilage. 2021;29(8):1155–62.
69. Puri T, Siddique MM, Frost ML, Moore AEB, Blake GM. A Short Dynamic Scan Method of Measuring Bone Metabolic Flux Using [18F]NaF PET. Tomography. 2021;7(4):623–35.
70. Wolf FA, Angerer P, Theis FJ. SCANPY: large-scale single-cell gene expression data analysis. Genome Biol. 2018;19:1–5.
71. Korsunsky I, Millard N, Fan J, Slowikowski K, Zhang F, Wei K, et al. Fast, sensitive and accurate integration of single-cell data with Harmony. Nat Methods. 2019;16(12):1289–96.
72. Trapnell C, Cacchiarelli D, Grimsby J, Pokharel P, Li S, Morse M, et al. The dynamics and regulators of cell fate decisions are revealed by pseudotemporal ordering of single cells. Nat Biotechnol. 2014;32(4):381–6.
73. Qiu X, Mao Q, Tang Y, Wang L, Chawla R, Pliner HA, Trapnell C. Reversed graph embedding resolves complex single-cell trajectories. Nat Methods. 2017;14(10):979–82.
74. Gulati GS, Sikandar SS, Wesche DJ, Manjunath A, Bharadwaj A, Berger MJ, et al. Single-cell transcriptional diversity is a hallmark of developmental potential. Science. 2020;367(6476):405–11.
75. Wu Y, Yang S, Ma J, Chen Z, Song G, Rao D, et al. Spatiotemporal immune landscape of colorectal cancer liver metastasis at single-cell level. Cancer Discov. 2022;12(1):134–53.
76. Single-cell transcriptomic study of ADO2 bone marrow cells. 2025. NCBI: https://www.ncbi.nlm.nih.gov/bioproject/PRJNA1219686.
77. Ou, M. LC-MS/MS-based 4D Label-Free N-Glycosylation Proteomics Analysis of Bone Marrow Cells from ADO2 Mouse. 2025. iProX: https://www.iprox.cn/page/project.html?id=IPX0011013000.
78. Ou, M. LC-MS/MS-based 4D Label-Free Proteomics Analysis of Bone Marrow Cells from ADO2 Mice. 2025. iProX: https://www.iprox.cn/page/project.html?id=IPX0011019000.

Publisher's Note